47th AIAA Aerospace Sciences Meeting Including The New Horizons Forum and Aerospace Exposition
5 - 8 January 2009, Orlando, Florida

AIAA 2009-402

Large Eddy Simulation of Compressible Turbulent Channel Flow with Spectral Difference method

Chunlei Liang, * Sachin Premasuthan, † and Antony Jameson ‡
Stanford University, Stanford, CA 94305, USA

Z.J.Wang§
Iowa State University, IA 50010, USA

This paper presents the development of a three-dimensional high-order solver with unstructured spectral difference method. The solver employs the formulations of Sun et al.[22] It is implemented on unstructured hexahedral grid elements. It is firstly validated using test problems of 2D and 3D subsonic inviscid flows past a circular cylinder. The spectral difference method constructs element-wise continuous fields. Five different types of Riemann solvers are employed to deal with the discontinuity across elements. We demonstrate the spatial accuracy up to fourth-order using the viscous compressible Couette flow with analytic solution. The 3D SD method is finally applied to a compressible turbulent channel flow at $Re_\tau = 400$. The predicted mean and r.m.s velocity profiles are in good agreement with DNS results of Moser et al.[15]

I. Introduction

The increase in computational power is enabling three-dimensional simulations of various research problems previously deemed intractable such as unsteady Large Eddy Simulation (LES) and Aero-acoustics. In LES, the smallest resolved scales are often used to model the contribution from the unresolved scales. Therefore, it is of great importance that these small scales are resolved to high accuracy. High accuracy LES results can be achieved by high-order numerical methods.[3] The need for highly accurate methods in applications such as large eddy simulation, direct numerical simulation, computational aero-acoustics etc. on complex geometries, has been the driving force for the development of higher order schemes for unstructured meshes such as the Discontinuous Galerkin (DG) Method,[1] Spectral Volume (SV) method[12,25] and Spectral Difference (SD) Method.[11,24] The SD method is a newly developed efficient high-order approach based on differential form of the governing equation. It was originally proposed by Liu et al[11] and developed for wave equations in their paper on triangular grids. Wang et al[24] extended it to 2D Euler equations on triangular grids and Sun et al[22] further developed it for three-dimensional Navier-Stokes equations on hexahedral unstructured meshes. The SD method combines elements from finite-volume and finite-difference techniques. The method is particularly attractive because it is conservative, and has a simple formulation and easy to implement.

Sheared turbulent channel flow contains many inhomogeneous and anisotropic large scales. Direct numerical simulations of compressible turbulent channel flow have been studied using structured-grid methods.[2,6,13,14] In this paper, we study the compressible turbulent channel flow using an unstructured grid method with high-order accuracy. In the following sections, we will firstly describe the numerical formulation of the high-order spectral difference method. Prior to its application to turbulent channel flow, we will validate the spectral difference method code using 2D and 3D inviscid flows past a cylinder as well as a viscous Couette flow.

*Postdoc, Department of Aeronautics and Astronautics, Stanford University, AIAA Member.
†Doctoral Candidate, Department of Aeronautics and Astronautics, Stanford University, AIAA Member.
‡Professor, Department of Aeronautics and Astronautics, Stanford University, AIAA Fellow.
§Professor, Department of Aerospace Engineering, Iowa State University, AIAA associate Fellow.

II. Numerical Formulation

The formulations of the equations employed in this paper are largely similar to the formulations of Sun et al[22] for unstructured hexahedral grids. Consider the unsteady compressible 3D Navier Stokes equations in conservative form

$$\frac{\partial Q}{\partial t} + \frac{\partial F}{\partial x} + \frac{\partial G}{\partial y} + \frac{\partial H}{\partial z} = 0 \tag{1}$$

where Q is the vector of conserved variables; F, G and H are the total fluxes including both inviscid and viscous flux vectors. To achieve an efficient implementation, all elements in the physical domain (x, y, z) are transformed into a standard square element ($0 \leq \xi \leq 1$, $0 \leq \eta \leq 1$ and $0 \leq \beta \leq 1$).

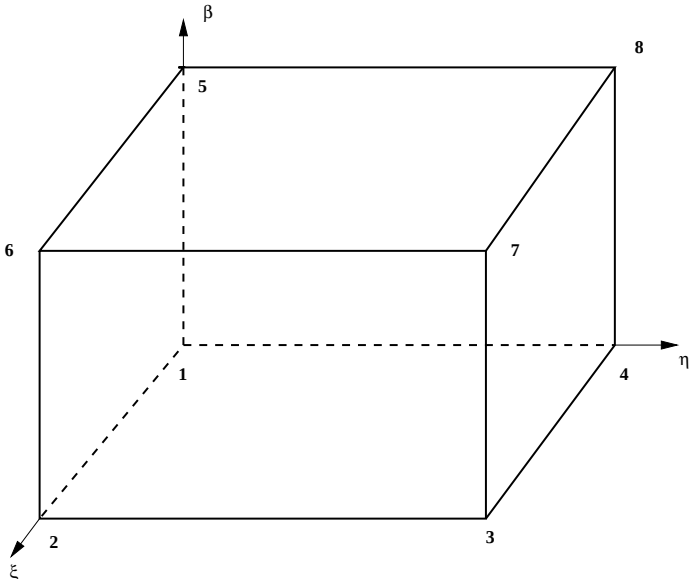

Figure 1. The nodal points and standard 3D cell orientation

The transformation can be written as:

$$\begin{pmatrix} x \\ y \\ z \end{pmatrix} = \sum_{i=1}^{K} M_i(\xi, \eta, \beta) \begin{pmatrix} x_i \\ y_i \\ z_i \end{pmatrix} \tag{2}$$

where K is the number of points used to define the physical element, (x_i, y_i, z_i) are the cartesian coordinates at those points, and $M_i(\xi, \eta, \beta)$ are the shape functions. For present implementation, we define K as 8 nodal points illustrated in figure 1. Nodal point 1 location is ($\xi = 0$, $\eta = 0$, $\beta = 0$). The metrics and the Jacobian of the transformation can be computed for each element. The Jacobian is can be expressed as:

$$J = \begin{pmatrix} x_\xi & x_\eta & x_\beta \\ y_\xi & y_\eta & y_\beta \\ z_\xi & z_\eta & z_\beta \end{pmatrix} \tag{3}$$

The governing equations in the physical domain are then transferred into the computational domain, and the transformed equations take the following form:

$$\frac{\partial \tilde{Q}}{\partial t} + \frac{\partial \tilde{F}}{\partial \xi} + \frac{\partial \tilde{G}}{\partial \eta} + \frac{\partial \tilde{H}}{\partial \beta} = 0 \tag{4}$$

where $\tilde{Q} = |J| \cdot Q$ and

$$\begin{pmatrix} \tilde{F} \\ \tilde{G} \\ \tilde{H} \end{pmatrix} = |J| J^{-1} \begin{pmatrix} F \\ G \\ H \end{pmatrix} \tag{5}$$

In the standard element, two sets of points are defined, namely the solution points and the flux points, illustrated in figure 2.

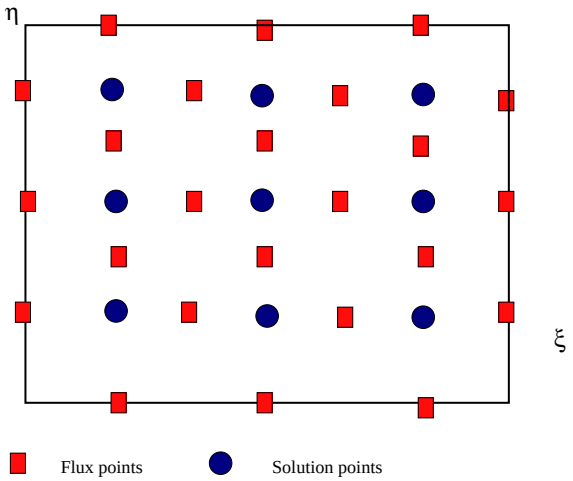

Figure 2. Distribution of flux and solution points for the third order SD scheme

In order to construct a degree $(N-1)$ polynomial in each coordinate direction, solution at N points are required. The solution points in 1D are chosen to be the Gauss points defined by:

$$X_s = \frac{1}{2}\left[1 - cos\left(\frac{2s-1}{2N}\cdot\pi\right)\right], s = 1, 2, \cdots, N. \tag{6}$$

The flux points are selected by Sun et al[22] as the Gauss-Lobatto points given by

$$X_{s+1/2} = \frac{1}{2}\left[1 - cos\left(\frac{s}{N}\cdot\pi\right)\right], s = 0, 1, \cdots, N. \tag{7}$$

For the computations in this paper, however, the flux points were selected to be Legendre-Gauss quadrature points plus the two end points 0 and 1, as suggested by Huynh.[7] Choosing $P_{-1}(\xi) = 0$ and $P_0(\xi) = 1$, we can determine the higher-degree Legendre polynomials as

$$P_n(\xi) = \frac{2n-1}{n}(2\xi - 1)P_{n-1}(\xi) - \frac{n-1}{n}P_{n-2}(\xi) \tag{8}$$

The locations of these Legendre-Gauss quadrature points are the roots of equation $P_n(\xi) = 0$. They are generally found to be more stable than the Gauss-Lobatto flux points.

Using the solutions at N solution points, a degree $(N-1)$ polynomial can be built using the following Lagrange basis defined as:

$$h_i(X) = \prod_{s=0, s\neq i}^{N}\left(\frac{X - X_s}{X_i - X_s}\right) \tag{9}$$

Similarly, using the fluxes at $(N+1)$ flux points, a degree N polynomial can be built for the flux using a similar Lagrange basis defined as:

$$l_{i+1/2}(X) = \prod_{s=0, s\neq i}^{N}\left(\frac{X - X_{s+1/2}}{X_{i+1/2} - X_{s+1/2}}\right) \tag{10}$$

The reconstructed solution for the conserved variables in the standard element is just the tensor products of the three one-dimensional polynomials,

$$Q(\xi, \eta, \beta) = \sum_{k=1}^{N}\sum_{j=1}^{N}\sum_{i=1}^{N}\frac{\tilde{Q}_{i,j,k}}{|J_{i,j,k}|}h_i(\xi)\cdot h_j(\eta)\cdot h_k(\beta) \tag{11}$$

Similarly, the reconstructed flux polynomials take the following form:

$$\begin{aligned}
\tilde{F}(\xi,\eta,\beta) &= \sum_{k=1}^{N}\sum_{j=1}^{N}\sum_{i=0}^{N}\tilde{F}_{i+1/2,j,k}l_{i+1/2}(\xi)\cdot h_j(\eta)\cdot h_k(\beta),\\
\tilde{G}(\xi,\eta,\beta) &= \sum_{k=1}^{N}\sum_{j=0}^{N}\sum_{i=1}^{N}\tilde{G}_{i,j+1/2,k}h_i(\xi)\cdot l_{j+1/2}(\eta)\cdot h_k(\beta),\\
\tilde{H}(\xi,\eta,\beta) &= \sum_{k=0}^{N}\sum_{j=1}^{N}\sum_{i=1}^{N}\tilde{H}_{i,j,k+1/2}h_i(\xi)\cdot h_j(\eta)\cdot l_{k+1/2}(\beta)
\end{aligned} \tag{12}$$

The reconstructed fluxes are only element-wise continuous, but discontinuous across cell interfaces. For the inviscid flux, a Riemann solver is employed to compute a common flux at interfaces to ensure conservation and stability. In our case, we have used the Riemann solvers such as Rusanov,[17] Roe[16] with entropy fix,[4] CUSP,[8] Flux vector splitting[20] and AUSM[10] schemes to compute the interface fluxes.

In summary, the algorithm to compute the inviscid flux derivatives consists of the following steps:

1. Given the conservative variables at the solution points, the conservative variables are computed at the flux points. The inviscid fluxes at the interior flux points can also be determined from the polynomials based on the solution points.

2. The inviscid fluxes at the element interfaces are computed using the Riemann solver. Given the normal direction of the interface n, and the averaged normal velocity component V_n and the sound speed c, the inviscid flux on the interface can be determined.

3. The derivatives of the inviscid fluxes are computed at the solution points using the derivatives of Lagrange operators l

$$\begin{aligned}
\left(\frac{\partial\tilde{F}}{\partial\xi}\right)_{i,j} &= \sum_{r=0}^{N}\tilde{F}_{r+1/2,j}\cdot l'_{r+1/2}(\xi_i),\\
\left(\frac{\partial\tilde{G}}{\partial\eta}\right)_{i,j} &= \sum_{r=0}^{N}\tilde{G}_{i,r+1/2}\cdot l'_{r+1/2}(\eta_j),\\
\left(\frac{\partial\tilde{H}}{\partial\beta}\right)_{i,j,k} &= \sum_{r=0}^{N}\tilde{H}_{i,j,r+1/2}\cdot l'_{r+1/2}(\beta_k)
\end{aligned} \tag{13}$$

4. The convective term $\nabla F_e(Q)$ can be readily determined after transforming these derivatives back the physical domain.

The conservative variables Q and Cartesian components $f_e(Q)$, $g_e(Q)$ and $h_e(Q)$ of the inviscid flux vector $F_e(Q)$ are given by

$$Q=\begin{Bmatrix}\rho\\ \rho u\\ \rho v\\ \rho w\\ E\end{Bmatrix},\quad f_e(Q)=\begin{Bmatrix}\rho u\\ \rho u^2+p\\ \rho uv\\ \rho uw\\ u(E+p)\end{Bmatrix} \tag{14}$$

$$g_e(Q)=\begin{Bmatrix}\rho v\\ \rho uv\\ \rho v^2+p\\ \rho vw\\ v(E+p)\end{Bmatrix},\quad h_e(Q)=\begin{Bmatrix}\rho w\\ \rho uw\\ \rho vw\\ \rho w^2+p\\ w(E+p)\end{Bmatrix} \tag{15}$$

Here ρ is the density, u, v and w are the velocity components in x, y and z directions, p stands for pressure and E is the total energy. The pressure is related to the total energy by

$$E = \frac{p}{\gamma - 1} + \frac{1}{2}\rho(u^2 + v^2 + w^2) \tag{16}$$

with a constant ratio of specific heat γ. For all test cases in the present study, γ is going to be 1.4 for air.

Three-dimensional Navier-Stokes equations have an additional viscous term dependent on not only conservative variables but also their gradients. To illustrate the treatment of viscous flow terms, one can write the Navier-Stokes equations in conservation terms as

$$\frac{\partial Q}{\partial t} + \nabla F_e(Q) - \nabla F_v(Q, \nabla Q) = 0 \tag{17}$$

The Cartesian components $f_v(Q, \nabla Q)$, $g_v(Q, \nabla Q)$ and $h_v(Q, \nabla Q)$ of viscous flux vector $F_v(Q, \nabla Q)$ are given by

$$f_v(Q, \nabla Q) = \left\{ \begin{array}{c} 0 \\ \tau_{xx} \\ \tau_{yx} \\ \tau_{zx} \\ u\tau_{xx} + v\tau_{yx} + w\tau_{zx} + \frac{\mu C_p}{P_r} T_x \end{array} \right\},$$

$$g_v(Q, \nabla Q) = \left\{ \begin{array}{c} 0 \\ \tau_{xy} \\ \tau_{yy} \\ \tau_{zy} \\ u\tau_{xy} + v\tau_{yy} + w\tau_{zy} + \frac{\mu C_p}{P_r} T_y \end{array} \right\},$$

$$h_v(Q, \nabla Q) = \left\{ \begin{array}{c} 0 \\ \tau_{xz} \\ \tau_{yz} \\ \tau_{zz} \\ u\tau_{xz} + v\tau_{yz} + w\tau_{zz} + \frac{\mu C_p}{P_r} T_z \end{array} \right\} \tag{18}$$

where μ is the dynamic viscosity, C_p is the specific heat and P_r stands for Prandtl number. T is temperature which can be derived from the perfect gas assumption. λ is set to $-2/3$ according to the Stokes hypothesis.

$$\begin{aligned} \tau_{xy} \equiv \tau_{yx} = \mu(v_x + u_y), \quad & \tau_{xz} \equiv \tau_{zx} = \mu(w_x + u_z), \\ \tau_{yz} \equiv \tau_{zy} = \mu(w_y + v_z), \quad & \tau_{xx} = 2\mu \left\{ u_x - \tfrac{u_x + v_y + w_z}{3} \right\}, \\ \tau_{yy} = 2\mu \left\{ v_y - \frac{u_x + v_y + w_z}{3} \right\}, \quad & \tau_{zz} = 2\mu \left\{ w_z - \tfrac{u_x + v_y + w_z}{3} \right\} \end{aligned}$$

The procedures to get viscous fluxes can be described as the following steps:

1. reconstruct Q_f at the flux points from the conservative variables at the solution points using equation (11).
2. average the field of Q_f on the element interfaces as $\overline{Q_f} = \frac{1}{2}(Q_f^L + Q_f^R)$. For interior flux points, $\overline{Q_f} = Q_f$. Meanwhile, appropriate boundary conditions shall be applied for specific edge flux points.
3. evaluate ∇Q at solution points from $\overline{Q_f}$ using equation (13) where $\nabla Q = \left\{ \begin{array}{c} Q_x \\ Q_y \\ Q_z \end{array} \right\}$ and $Q_x = \frac{\partial Q}{\partial \xi}\xi_x + \frac{\partial Q}{\partial \eta}\eta_x + \frac{\partial Q}{\partial \beta}\beta_x$, etc.

4. reconstruct ∇Q from solution points to flux points and using equation (11), average them on the element interfaces as $\overline{\nabla Q_f} = \frac{1}{2}(\nabla Q_f^L + \nabla Q_f^R)$

5. use $\overline{Q_f}$ and $\overline{\nabla Q_f}$ in order to compute the viscous flux vectors described in equation (18) at the element interfaces.

Flows with either steady or unsteady solutions are considered in this paper. All computations utilize a fourth-order accurate, strong-stability-preserving five-stage Runge-Kutta scheme.[19]

III. Validation studies

In the following, we are going to study 2D and 3D inviscid flows past a cylinder and a 3D viscous Couette flow.

III.A. Inviscid flow past a circle

Firstly, we compute 2D and 3D subsonic inviscid flows past a circular cylinder ($Mach = 0.2$). The three dimensional grid is generated after extruding a two-dimensional grid with 32×20 cells shown in figure 3 with three-cell thickness in the spanwise direction. Two-dimensional flow past a circle has been considered as a test problem for validating the DG[1] and SV[25] methods. Higher order curved wall representation was proved to be important for both DG and SV methods. In our simulations, a quadratic curved wall boundary condition is implemented for the inner circle. The inviscid fluxes on the wall are imposed as $\overline{f}_e(Q) = \begin{Bmatrix} 0 \\ p \cdot n_x \\ p \cdot n_y \\ p \cdot n_z \\ 0 \end{Bmatrix}$. Fixed-value Dirichlet boundary condition is used for the outer boundary of the grid. In the spanwise direction, a periodic boundary condition is employed. The Mach number contour obtained by the 4th order SD scheme for this potential flow problem is shown in figure 4. The CUSP scheme developed by Jameson[8] is used in this simulation. Nearly ideal symmetric patterns are successfully obtained.

In order to demonstrate the effect of Riemann solvers on the numerical solutions, five different flux formulations are implemented. Numerical tests are performed using the 4th-order SD method and a quadratic curved wall representation. The drag coefficients obtained by are very small for every Riemann solver as shown in table 1. The Rusanov solver produces an accurate drag coefficient with the smallest magnitude.

Table 1. Drag coefficients predicted by the SD method with different Riemann solvers

Riemann	order	cell no.	Wall	Mach	$\Delta_t u_\infty / D$	C_d
CUSP[8]	4th	640	quadratic	0.2	2e-4	-1.86e-5
AUSM[10]	4th	640	quadratic	0.2	2e-4	-4.39e-5
Roe[16]	4th	640	quadratic	0.2	2e-4	-1.03e-5
Vector split[20]	4th	640	quadratic	0.2	2e-4	-1.18e-5
Rusanov[17]	4th	640	quadratic	0.2	2e-4	-8.8e-6

In particular, choosing the Gauss-Lobatto points, the SD methods produce instable solutions for 2D and 3D simulations of the inviscid flow past a cylinder. In contrast, the choice of Legendre-Gauss quadrature points plus the two end points produces stable and accurate 2D and 3D results as presented in this paper.

III.B. 3D viscous planar Couette flow

The numerical order of accuracy is validated using a compressible Couette flow with analytical solution. A grid with $6 \times 3 \times 3$ cells is shown in figure 5 (a). A periodic boundary condition is used in the stream-wise direction. A moving wall no-slip boundary with constant temperature and a specified external pressure is used for the top surface ($y = H$). A stationary no-slip wall with constant temperature is used for the bottom

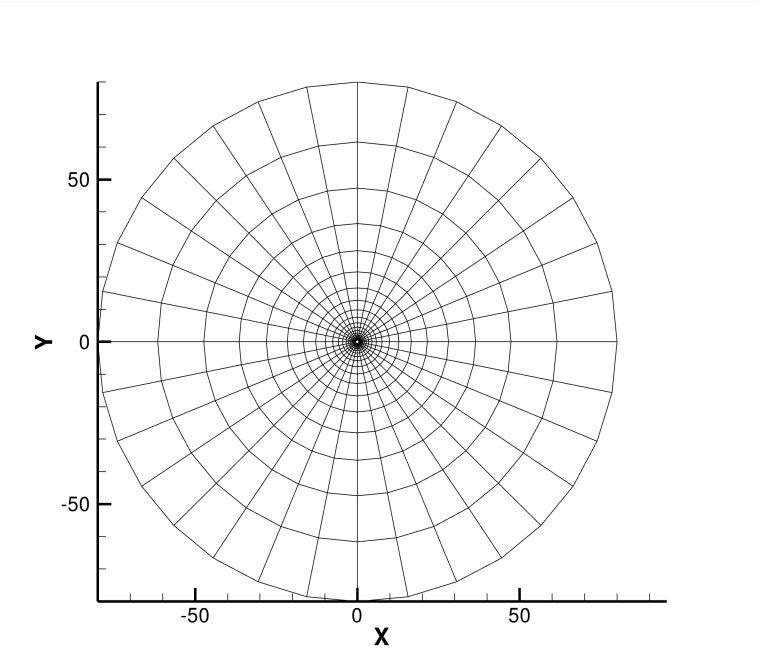

Figure 3. Grid $32 \times 20 \times 3$ for inviscid flow past a circular cylinder

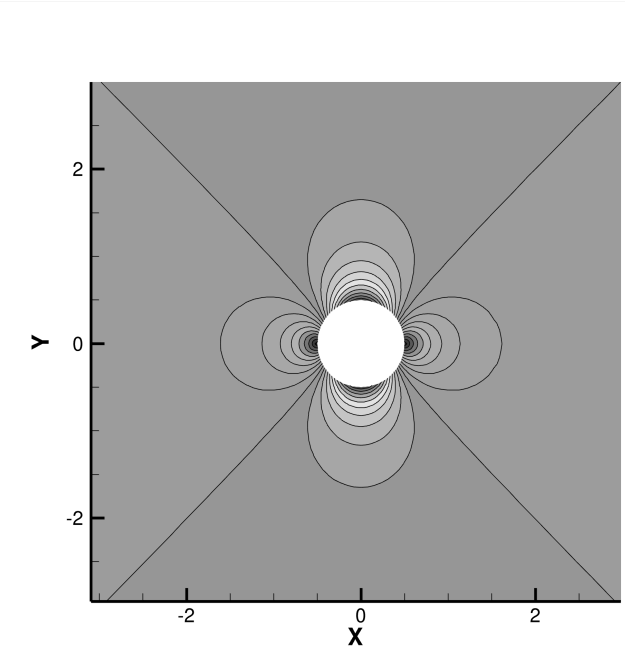

Figure 4. Mach number contour obtained for inviscid flow past a circular cylinder using 4th-order SD method and quadratic curved wall boundary

surface $y = 0$. In the spanwise direction, periodic boundary condition is again implemented. The exact solutions of the this problem are

$$u = \frac{U}{H}y, \qquad v = 0, \qquad w = 0;$$
$$e = e_b + \frac{y}{H}(e_t - e_b) + \frac{PrU^2}{2\gamma}\frac{y}{H}(1 - \frac{y}{H}); \quad p = const$$

Where Pr is the Prandtl number and $e = C_v T$ is the internal energy. The density ρ is related to pressure p through $\rho = \frac{p}{(\gamma-1)e}$ The subscripts t and b refer to top and bottom surfaces respectively.

We obtained desired numerical order up to 4th order accuracy using $L2$ error as shown in table 2. It demonstrates that the basic implementations of the three-dimensional Spectral Difference method are successful. A typical solution of density ρ is shown in figure 5 (b), and it is a quadratic function of y.

No. of elements	No. of DOFs	L2-error	Order
2nd order SD			
2	16	1.25E-02	-
16	128	2.65E-03	2.24
54	432	9.62E-04	2.49
3rd order SD			
2	54	1.46E-03	-
16	432	1.18E-04	3.60
54	864	2.48E-05	3.85
4th order SD			
2	128	1.73E-04	-
16	1024	9.79E-06	4.14
54	3456	1.93E-06	4.01

Table 2. L^2 errors and orders of accuracy of viscous Couette flow

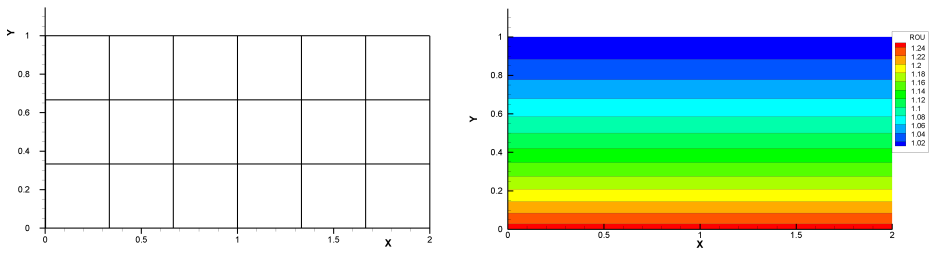

(a) Grid $6 \times 3 \times 3$ (b) density contour

Figure 5. Compressible Couette flow grid and its solution for density field.

IV. Application to turbulent channel flow

For compressible turbulent channel flow, a uniform fictitious body force $\frac{-\tau_w \rho \delta_1}{\rho_b H}$ term is added into the x-momentum equation of the Navier-Stokes equation similar to the previous DNS studies of the compressible turbulent channel flow.[6,13] Although the body force has the same function as the one in the DNS of incompressible turbulent channel flow, it is not interpreted as the mean pressure gradient. The pressure term in our case is given the state equation (16). The computational box lengths are $6.4\delta \times 2\delta \times 3.2\delta$ and δ is the half channel width. As shown in figure 6, the computational grid has $24 \times 40 \times 12$ cells in x, y and z directions respectively. Periodic boundary conditions are employed for streamwise and spanwise directions. Iso-thermal wall conditions are imposed on the boundaries in the wall-normal directions.

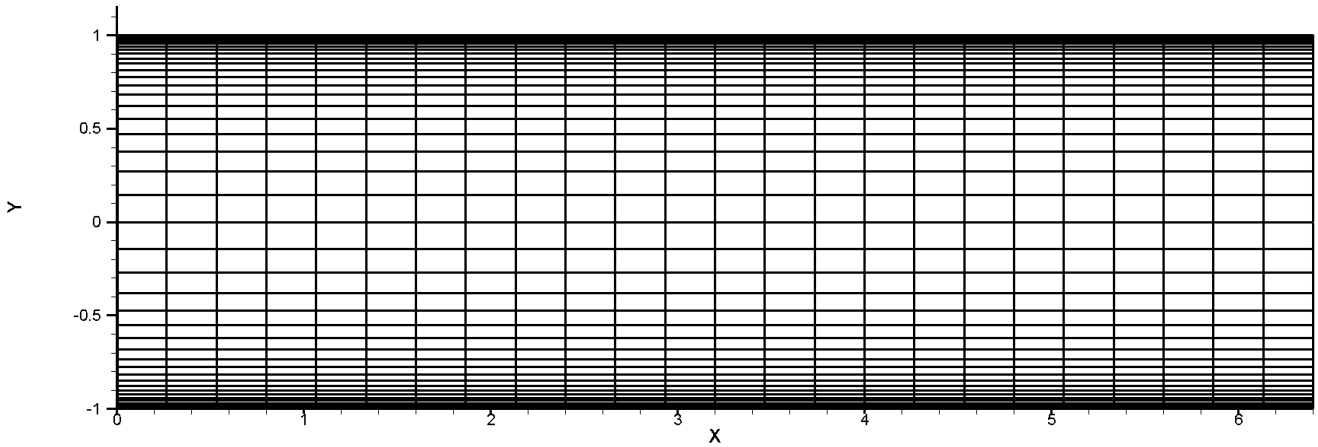

Figure 6. Computational grid for channel flow $24 \times 40 \times 12$

IV.A. Solving Orr-Sommerfeld equation using a 4th order finite difference method

Small disturbances imposed to the corresponding 2D Navier-Stokes equation of a plane Poiseuille flow lead to an eigenvalue problem for the Orr-Sommerfeld equation with given boundary conditions. The Orr-Sommerfeld instability equation is

$$\frac{d^4\phi}{dy^4} - 2\alpha^2\frac{d^2\phi}{dy^2} + \alpha^4\phi - i\alpha Re_c\left\{(\overline{u} - C)\left(\frac{d^2\phi}{dy^2} - \alpha^2\phi\right) - \frac{d^2\overline{u}}{dy^2}\phi\right\} = 0 \tag{19}$$

where C is the complex phase velocity of the disturbance, α is the streamwise wavenumber, and Reynolds number $Re_c = \frac{U_c\delta}{\nu}$ is based on the centerline velocity U_c and channel half length δ. This Reynolds number is approximately equal to 20887.5 to match conditions for the presently considered Reynolds number $Re_\tau = 400$. The laminar streamwise velocity solution is given as

$$\overline{u} = U_c\left(1 - \eta^2\right) \tag{20}$$

where, $\eta = y/\delta$.

Non-slip wall boundary conditions are used at the top and bottom planes $|\eta| = 1$ as $\phi = 0$ and $\frac{d\phi}{dy} = 0$, the symmetrical boundary conditions are applied at the centerline $\eta = 0$ as $\frac{d\phi}{dy} = 0$ and $\frac{d^3\phi}{dy^3} = 0$.

In particular, we take the following formulation used by Thomas[23] in order to obtain a more accurate difference equation

$$f = \phi - \frac{1}{6}\Delta y^2\frac{d^2\phi}{dy^2} + \frac{1}{90}\Delta y^4\frac{d^4\phi}{dy^4}. \tag{21}$$

The Orr-Sommerfeld equation is then transformed to a linear system as

$$\mathcal{A}\mathcal{F} = \mathcal{R} \tag{22}$$

where $\mathcal{A}$ is an $N \times N$ matrix, $\mathcal{F}$ is a N element vector f and $\mathcal{R}$ is a vector of N elements set as zero, except the first element set as 1.

Fully pivoting Gauss-Jordan scheme is used to get upper triangular matrix and obtain the solution of the linear system. The Newton method is used to search new complex number C in order to make the $\mathcal{A}$ matrix singular.

Given different value of the streamwise wavenumber α, we solve the Orr-Sommerfeld equation and obtain the most instable eigenvalue accordingly. The streamwise wavenumber 1.0 is chosen in order to fit the streamwise length of the channel. After adjusting $\phi|_{\eta=0} = 1$ for normalization, the final eigen-solutions of the Orr-Sommerfeld equation are obtained in figures (7) and (8) for real and imaginary parts against η from 0 to 1.

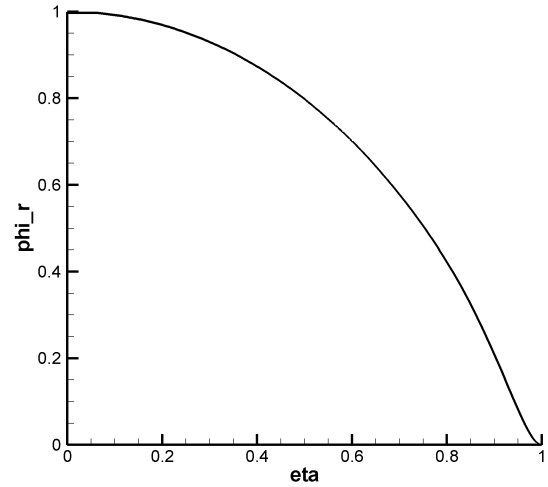

Figure 7. The eigen-solution of the Orr-Sommerfeld equation (real part)

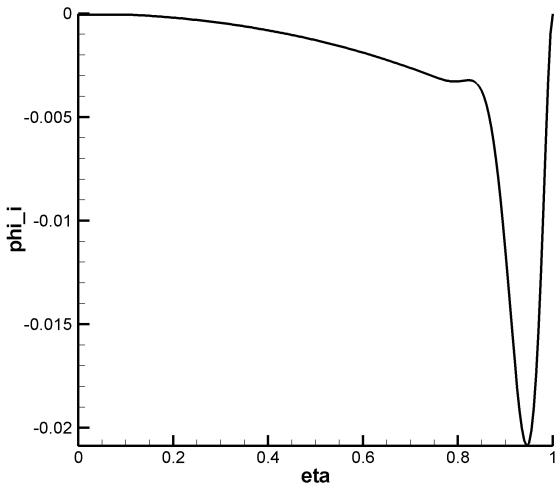

Figure 8. The eigen-solution of the Orr-Sommerfeld equation (imaginary part)

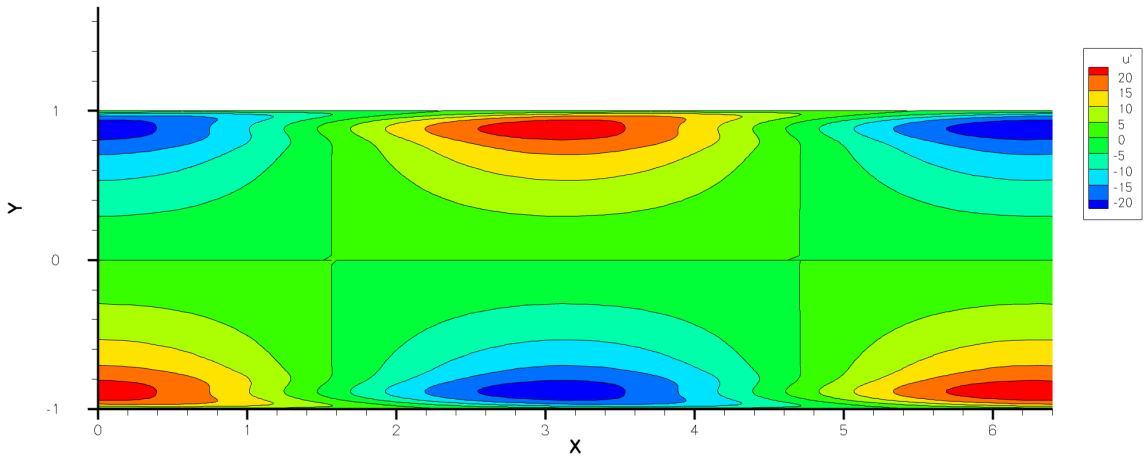

Figure 9. The imposed streamwise perturbation velocity field contour

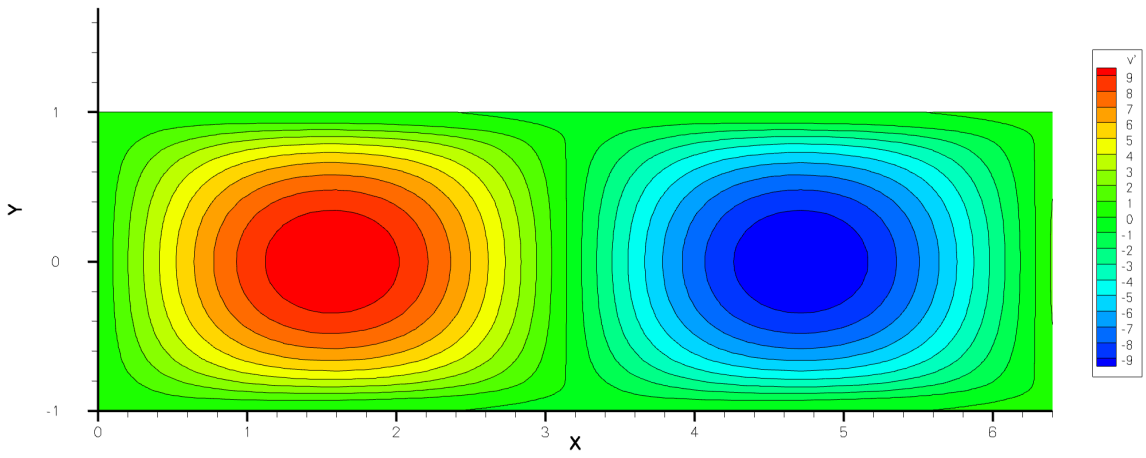

Figure 10. The imposed wall-normal perturbation velocity field contour

The streamfunction of perturbation field is given as

$$\psi = \phi(\eta)e^{i(kx-\omega t)} \tag{23}$$

where $\omega = C\alpha U_c/\delta$. Thus we can evaluate the velocity disturbance using the following relationships

$$u' = \frac{\partial \psi}{\partial y} = \frac{d\phi(\eta)}{dy}e^{i(kx-\omega t)} \tag{24}$$

$$v' = -\frac{\partial \psi}{\partial x} = -ik\phi(\eta)e^{i(kx-\omega t)} \tag{25}$$

The disturbance is imposed on the laminar solution of the plane Poiseuille flow as

$$\begin{aligned} u &= \overline{u} + \epsilon u'; \\ v &= \epsilon v' \end{aligned} \tag{26}$$

where ϵ is a small number normally less than 1 to ensure that the small disturbance imposed on the laminar flow solution is relatively very small (ϵ is 0.01 for this case). The determined perturbation fields are shown in figure (9) for u' and figure (10) for v'.

IV.B. Turbulent channel flow statistics

Turbulence in channel flow is generated primarily from the wall shear stresses. Reynolds-averaged Navier-Stokes (RANS) methods have generally been unsuccessful in predicting the turbulence. Large eddy simulation with second-order spatial accuracy using the Smagorinsky model[18] requires von Driest damping function to artificially reduce the eddy viscosity near the wall. Gullbrand and Chow[3] reported that a fourth-order accurate finite-difference scheme obtained much more accurate results than a second-order finite-difference scheme and could produce moderately accurate results on a Cartesian grid without any turbulence modeling.

Using the computational grid of $24 \times 40 \times 12$ elements mentioned above, the computation was firstly performed using the third-order SD scheme. The initial conditions are obtained from the parabolic profiles of the plane Poiseuille flow with further super-imposition of the determined perturbation fields u' and v'. The computation was performed on a serial computer for about 10 days. The solutions obtained using the third SD method are employed as the initial conditions for the fourth-order SD method. The final statistics is obtained by the the 4th-order SD method on the same grid with a total number of degrees-of-freedom of 737,280 for each independent variable. The computation employs a non-dimensional time step size $\Delta t \times u_\tau/\delta = 5.94e-5$. The averaged Mach number is around 0.4 and the flow is subsonic. The statistics is collected over a period of $t \times u_\tau/\delta = 1.07$ after the turbulent flow becomes fully-developed.

The simulations produce instantaneous turbulent structures resembling streaks on the layer at a height 0.03δ above the wall where δ is the half channel width, as shown in figure 11 . In addition, coherent structures in the spanwise vorticity are also captured on a middle x-y plane as shown in figure 12. The SD results compare very well with the direct numerical simulation of Moser et al[15] using 9,486,336 nodes. The velocity profiles are presented in figure 13 against the DNS results. The peak of the mean streamwise velocity profile is slightly over-predicted by the SD method against the DNS results. The streamwise and wall-normal r.m.s velocities u^+_{rms} and v^+_{rms} predicted by the SD method agree very well with the DNS results. The peak of the rms spanwise velocity is again slightly over-predicted by the SD method in figure 13(d).

V. Concluding Remark

A three-dimensional SD unstructured solver suitable for Large Eddy Simulation has been developed for viscous compressible flows. 2D and 3D solvers are successfully applied to compute subsonic inviscid 2D and 3D flow past a circular cylinder. The predicted flow pattern is symmetric and the drag coefficients are of very small amplitudes regardless of the choice of Riemann solvers. We also verified that the solver on hexahedral grids could achieve the desired numerical order for a 3D compressible viscous Couette flow. Finally, the SD method is used to simulate a turbulent compressible channel flow at $Re_\tau = 400$. Small perturbations generated from the Orr-Sommerfeld equation are imposed on the laminar parabolic velocity profiles to successfully accelerate the transition to fully three-dimensional turbulent state. The profiles predicted by the 4th-order SD method are in very good agreement for both mean and r.m.s velocity profiles with the DNS results obtained by Moser et al[15] at a similar Reynolds number.

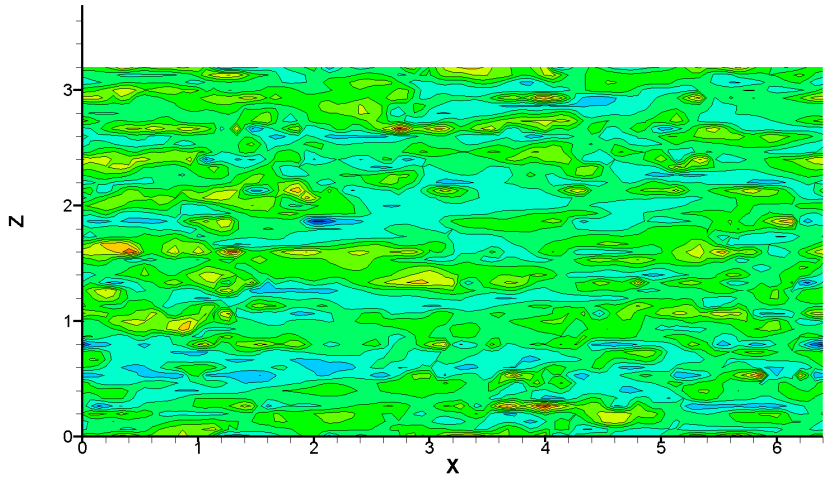

Figure 11. Streamwise velocity streams at 0.03δ above channel wall predicted by 4th-order SD method

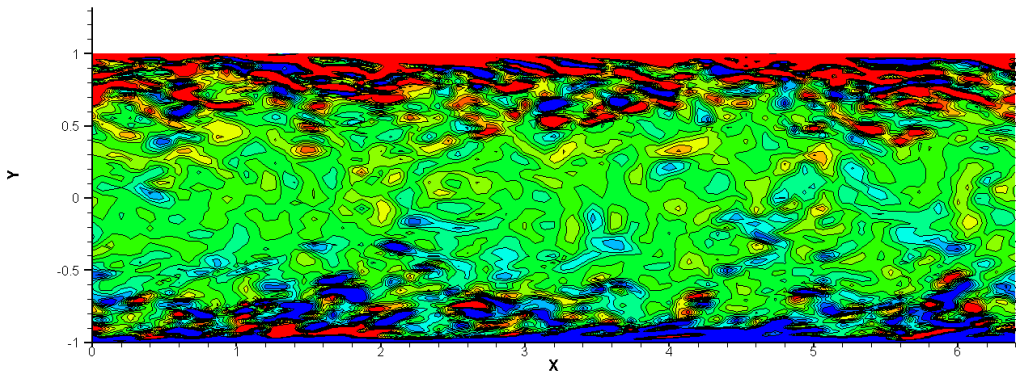

Figure 12. Spanwise vorticity contour on a middle plane in the spanwise direction predicted by the 4th-order SD method

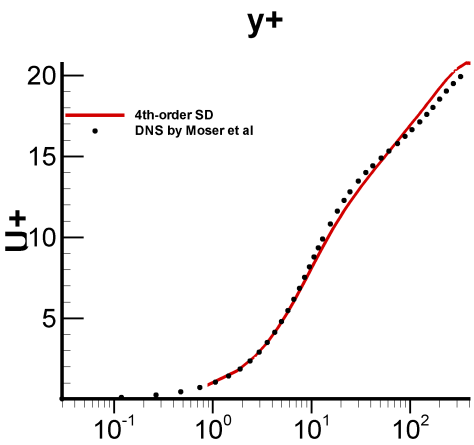

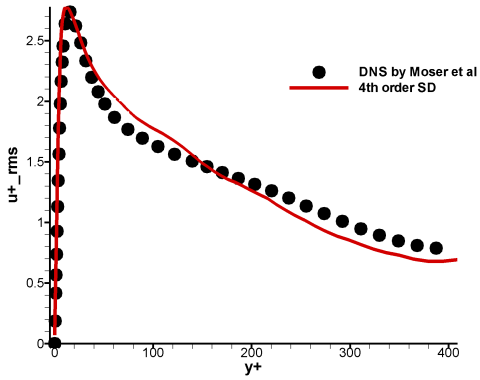

(a) plane averaged mean velocity $\overline{u}$ (b) plane averaged r.m.s velocity u^+_{rms}

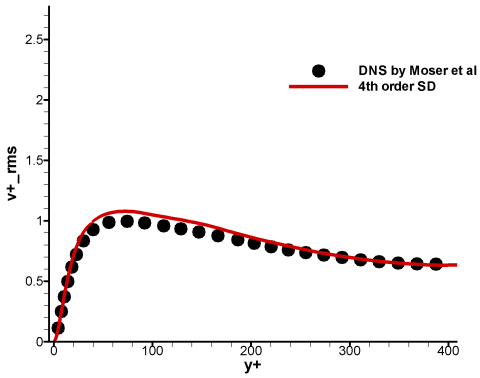

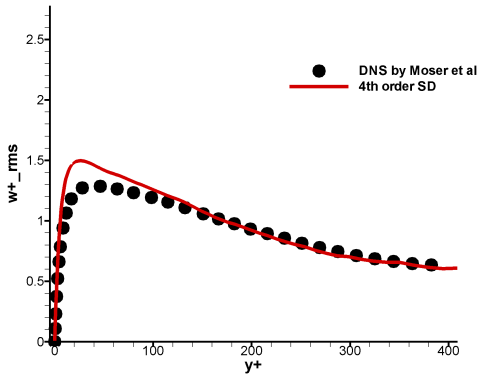

(c) plane averaged r.m.s velocity v^+_{rms} (d) plane averaged r.m.s velocity w^+_{rms}

Figure 13. Prediction by 4th order SD method against DNS data by Moser et al.

References

[1]F.Bassi and S. Rebay, High-order accurate discontinuous finite element solution of the 2D euler equations, *Journal of Computational Physics*, Vol. 138, pp. 251-285, 1997

[2]G. N. Coleman, J. Kim, & R. D. Moser, A numerical study of turbulent supersonic isothermal-wall channel flow, *Journal of Fluid Mechanics*, Vol 305, pp. 159-183, 1995

[3]J. Gullbrand and F. K. Chow, The effect of numerical errors and turbulence models in large-eddy simulations of channel flow, with and without explicit filtering, *Journal of Fluid Mechanics*, Vol 495, pp. 323-341, 2003.

[4]A. Harten, P. D. Lax and B. van Leer, On Upstream Differencing and Godunov-Type Schemes for Hyperbolic Conservation Laws, SIAM Rev, Vol 25, pp. 35-61, 1983.

[5]B. T. Helenbrook and H. L. Atkins, Application of p-Multigrid to Discontinuous Galerkin formulations of the Poisson equation, *AIAA Journal*, Vol. 44, pp. 566-575, 2006.

[6]P. Huang, G. N. Coleman and P. Bradshaw, Compressible turbulent channel flow: DNS results and modelling, *Journal of Fluid Mechanics*, Vol 305, pp. 185-218, 1995

[7]H.T. Huynh, A Flux Reconstruction Approach to High-Order Schemes Including Discontinuous Galerkin Methods, *AIAA paper*, AIAA-2007-4079, 2007.

[8]A. Jameson, Time dependent calculations using multigrid, with applications to unsteady flows past airfoils and wings, *AIAA paper*, AIAA-1991-1596, 1991.

[9]C. Liang, R. Kannan & ZJ Wang, A p-Multigrid Spectral Difference Method with explicit and implicit smoothers on unstructured triangular grids, *Computers and Fluids*, Vol. 38, pp. 254-265, 2009.

[10]M. S. Liou and C. Steffen, A New Flux Splitting Scheme, *J. Comput. Phys.*, Vol. 107, pp. 23-39, 1993.

[11]Y. Liu, M. Vinokur, & Z. J. Wang, Spectral difference method for unstructured grids I: Basic formulation, *J. of Comput. Phys.*, Vol. 216 , pp. 780-801, 2006.

[12]Y. Liu, M. Vinokur, & Z. J. Wang, Spectral (finite) volume method for conservation laws on unstructured grids V: Extension to three-dimensional systems, *Journal of Computational Physics*, Vol. 212, pp 454-472, 2006.

[13]Y. Morinishi, S. Tamano and K. Nakabayashi, A DNS algorithm using B-spline collocation method for compressible turbulent channel flow, *Computers and Fluids*, Vol 32, pp. 751-776, 2003

[14]Y. Morinishi, S. Tamano and K. Nakabayashi, Direct numerical simulation of compressible turbulent channel flow between adiabatic and isothermal walls, *Journal of Fluid Mechanics*, Vol 502, pp. 273-308, 2004

[15]R. Moser, J. Moser and N. Mansour (1999) DNS of turbulent channel flow up to $Re_\tau = 590$. *Physics of Fluids*, Vol 11, pp. 943-945, 1999.

[16]P. L. Roe, Approximate riemann solvers, parameter vectors and difference schemes, *Journal of Computational Physics*, Vol 43, pp. 357-372, 1981.

[17]V.V. Rusanov, Calculation of interaction of non-steady shock waves with obstacles, *Journal of Computational and Mathematical Physics USSR*, Vol. 1, pp. 267279, 1961.

[18]J. Smagorinsky, General Circulation Experiments with the Primitive Equations. I. The Basic Experiment, *Mon. Weather Rev.*, Vol. 91, pp. 99164, 1963.

[19]R. J. Spiteri, S. J. Ruuth, A new class of optimal high-order strong-stability-preserving time discretization methods, *SIAM J. Numer. Anal.*, Vol 40, pp 469-491, 2002

[20]J. L. Steger and R. F. Warming, Flux vector splitting of the inviscid gasdynamic equations with application to finite-difference methods, *Journal of Compt. Physics*, Vol 40, pp. 263-293, 1981.

[21]Y. Sun, Z. J. Wang, & Y. Liu, Efficient Implicit LU-SGS Algorithm for high-order spectral difference method on unstructured hexahedral grids, *AIAA paper*, AIAA-2007-313, 2007.

[22]Y. Sun, Z. J. Wang, & Y. Liu, High-order multidomain spectral difference method for the Navier-Stokes equations on unstructured hexahedral grids, *Communication in Computational Physics*, Vol. 2, pp. 310-333, 2007.

[23]L. H. Thomas, The stability of plane Poiseuille flow, *Physical Review*, Vol 91, pp. 780-783, 1953

[24]Z.J. Wang, Y. Liu, G. May and A. Jameson, Spectral Difference Method for Unstructured Grids II: Extension to the Euler Equations, *Journal of Scientific Computing*, Vol. 32, pp. 45-71, 2007.

[25]Z. J. Wang & Y. Liu, Extension of the spectral volume method to high-order boundary representation, *Journal of Computational Physics*, Vol. 211, pp. 154-178, 2006.